Journal of Solid State Electrochemistry (2019) 23:63–72
https://doi.org/10.1007/s10008-018-4115-8

ORIGINAL PAPER

Microwave-assisted synthesis of Fe-doped $NiMnO_3$ as electrode material for high-performance supercapacitors

Shaoming Qiao[1] · Naibao Huang[1] · Junjie Zhang[1] · Yuanyuan Zhang[1] · Yin Sun[1] · Zhengyuan Gao[1]

Received: 24 July 2018 / Revised: 21 September 2018 / Accepted: 24 September 2018 / Published online: 30 September 2018

Abstract

Fe-doped $NiMnO_3$ nanosheet electrode material was successfully synthesized by convenient and efficient microwave-assisted hydrothermal method. The crystal structure, chemical composition, morphology, and specific surface area of the electrode material were analyzed by X-ray diffraction, Fourier transform infrared, X-ray photoelectron spectroscopy, scanning electron microscopy, transmission electron microscopy, and Brunner–Emmet–Teller testing. Results showed that Fe doping changed not only the crystal structure but also the morphology of the $NiMnO_3$ nanosheet electrode material. Moreover, the electrode material exhibited a high specific surface area and outstanding conductivity. Electrochemical performance was analyzed by cyclic voltammetry, galvanostatic charge–discharge, and electrochemical impedance spectroscopy. The outcome of these experiments demonstrated that the Fe-doped $NiMnO_3$ electrode material exhibited optimum electrochemical performance when the mass ratio was 15 wt%. The specific capacitance reached 732.7 F g^{-1} at a current density of 1 A g^{-1}, and capacitance retention was approximately 78.3% after 10,000 cycles at 3 A g^{-1}. The Fe-doped $NiMnO_3$ electrode material is thus a promising next-generation supercapacitor material because of its high specific capacitance and long cycle life.

Keywords Supercapacitor · Fe-doped $NiMnO_3$ · Electrode material · Microwave-assisted hydrothermal

Introduction

Owing to the increasing demand for energy and high utilization of nonrenewable resources, finding new energy sources and energy storage devices has become essential [1, 2]. Some novel energy storage devices, such as Li-ion batteries, and supercapacitors have emerged [3, 4]. Supercapacitors, known as electrochemical capacitors, have attracted considerable interest because of their long cycle lives, high power densities, and fast charging–discharging rates [5–7]. However, their low energy densities remain a major obstacle. According to the calculation formula for energy density ($E=\frac{CV^2}{2}$), energy density (E) can be enhanced by two strategies [8]. Some researchers focused on electrolytes or assembled an asymmetrical supercapacitor device to enlarge potential windows (V), while other researchers focused on increasing the specific surface area and conductivity of electrode materials to improve specific capacitance (C).

Electrode material is a key factor for the electrochemical performance of supercapacitors and is usually categorized as carbon-based materials [9], conducting polymers [10], and transition metal oxide/hydroxide [11]. Carbon-based materials store energy through ion reversible electrostatic adsorption at the electrode/electrolyte interfaces, such as activated carbon, carbon nanotubes, and graphene [12]. Carbon-based materials are widely used as electrode materials because of their high electronic conductivity, abundant reserves, and outstanding specific surface areas. Conducting polymers, such as polyaniline, polypyrrole, and polythiophene, have high pseudocapacitance and electrical conductivity [13–15]. However, conducting polymers often show poor electrochemical stability because their shapes easily change during long-time charging/discharging process. Transition metal oxide/hydroxide electrode materials possessing broad potential windows and high pseudocapacitance, such as NiO [16], MnO_2 [12], Co_3O_4 [17, 18], V_2O_5 [19, 20], and Fe_2O_3 [21], have gained considerable attention. However, they have lower electrical conductivity than carbon materials [16]. Measures for improving electrochemical performance have been proposed, such as synthesizing binary transition metal oxides, such as $NiCo_2O_4$ [22–24], $MnCo_2O_4$

✉ Naibao Huang
nbhuang@dlmu.edu.cn

[1] Department of Materials Science and Engineering, Dalian Maritime University, Dalian 116026, People's Republic of China

[25, 26], $ZnCo_2O_4$ [27, 28], $NiMoO_4$ [29]; fabricating composite structures and combining them with transition metal oxide/hydroxide and carbon-based materials or conducting polymers; and turning to metal sulfides [30].

One of the binary transition metal oxides, $NiMnO_3$, has attracted considerable attention. On the one hand, it possess higher theoretical specific capacitance and electrical conductivity than NiO and MnO_2 because of the two redox reactions of Mn^{4+}/Mn^{3+} and Ni^{3+}/Ni^{2+} on the electrode material. These reactions provide more electrons than the single reaction of Mn^{4+}/Mn^{3+} or Ni^{3+}/Ni^{2+}. On the other hand, it has simple and low-cost synthesis. Kakvand's group reported $NiMnO_3$/C composite electrode materials for capacitors with high specific capacitance of 285 F g^{-1} at 1 A g^{-1} and an excellent cycle stability of 93.5% at 2 A g^{-1} after 1000 charge–discharge cycles [31]. Giri et al. proved that $NiMnO_3$/"nitrogen-doped" graphene nanocomposites have good electrochemical performance at current density of 1 A g^{-1} and specific capacitance of 523.5 F g^{-1} [32]. Recently, some achievements have been made on $NiMnO_3$ electrode materials. Nevertheless, more efforts should be made for further developments.

In our work, we successfully synthesized Fe-doped $NiMnO_3$ nanosheet electrode materials by microwave-assisted hydrothermal method. Electrochemical testing showed that the optimum mass ratio was 15 wt% Fe, and its specific capacitance reached 732.7 F g^{-1} at a current density of 1 A g^{-1} in 6 mol L^{-1} KOH electrolyte. The specific capacitance retention reached approximately 78.3% after 10,000 cycles at 3 A g^{-1}. The as-prepared material is a potential candidate for next-generation supercapacitors.

Experimental

Synthesis of materials

All the reagents used in our work were of analytical grade and used directly without any further purification. According to the following process, the Fe-doped $NiMnO_3$ nanosheets were synthesized by microwave-assisted hydrothermal condition. First, 1 mmol $Ni(NO_3)_2{\cdot}6H_2O$, 1 mmol $KMnO_4$, 6 mmol NH_4F, and 12 mmol urea were dissolved in 30 mL of deionized water under continuous stirring for 30 min. Second, $Fe_2(SO_4)_3{\cdot}9H_2O$ was added into the solution, which was then stirred for an hour. The mass of $Fe_2(SO_4)_3{\cdot}9H_2O$ was X% (X = 0, 6, 9, 15, 20) of the sum mass of $Ni(NO_3)_2{\cdot}6H_2O$ and $KMnO_4$. Third, the solution was transferred into a Teflon-lined autoclave, which was specially used for microwave heating and occupied 30% of the total volume. Then the solution was treated at 160 °C for 3 h in XH-800G microwave hydrothermal reactor and cooled to room temperature. Finally, the Fe-doped $NiMnO_3$ nanosheet black powder was obtained after the solution was centrifuged, washed with deionized water and then with ethanol, dried for one night at 60 °C, and calcined in pipe furnace at 450 °C for 2 h. The $Fe_2(SO_4)_3{\cdot}9H_2O$ mass denoted the electrode materials as 0 wt%, 6 wt%, 9 wt%, 15 wt%, and 20 wt%, respectively.

Characterization

The crystal structural analysis of the obtained powder was examined by X-ray diffraction [XRD, Rigaku, D/MAX-Ultima$^-$ diffraction meter, using Co-Kα radiation (λ = 1.7902 Å)] ranging from 10 to 90° at a scan rate of 8°/min. The functional groups on the surface were tested by Fourier transform infrared (FT-IR) spectroscopy (Frontier, America). The chemical composition and distribution of products were determined by energy dispersive spectroscopy. The X-ray photoelectron spectroscopy (XPS) was conducted on Thermo ESCALAB 250 XPS system using Al-Kα radiation. The morphology and microstructure of the powder were determined by scanning electron microscopy (SEM, SUPRA 55 SAPPHHIRE) and transmission electron microscopy (TEM, JEOL JEM-2100). Brunner–Emmet–Teller (BET, WBL-810) was used to measure the specific surface area and pore size distribution of the samples.

Electrochemical measurement

The electrochemical performance were analyzed by cyclic voltammetry (CV), galvanostatic charge–discharge (GCD), and electrochemical impedance spectroscopy (EIS) on a VMP3 (EG&G) electrochemical workstation in 6 mol/L KOH electrolyte solution by a three-electrode system. The nickel foam coated by the black mud, which was composed of Fe-doped $NiMnO_3$ powder, conductive additive (XC-72), and binder (mass ratio of 75:15:10) as the working electrode, platinum net as counter electrode, and saturated calomel electrode as reference electrode. The binder was a mixture of polyvinylidene fluoride and N-methyl-2-pyrrolidone with weight ratio of 1:10. The loading mass of mud on nickel foam was approximately 2.5 mg/cm^2. EIS measurements were accomplished in the frequency range of 0.01 Hz to 100 kHz at open circuit potential. Using CV and GCD curves, specific capacitance (C) was calculated using Eqs. (1) and (2). Equation (3) is the Debye–Scherrer equation:

$$C = \frac{1}{2mv(Vc-Va)}\int_{Va}^{Vc} I(V)dV \tag{1}$$

$$C = \frac{I\Delta T}{m\Delta V} \tag{2}$$

$$D = \frac{K\gamma}{B\cos\theta} \tag{3}$$

where C is the specific capacitance (F g^{-1}), ν is the potential scan rate (mV s^{-1}), ($V_c - V_a$) and (ΔV) are the

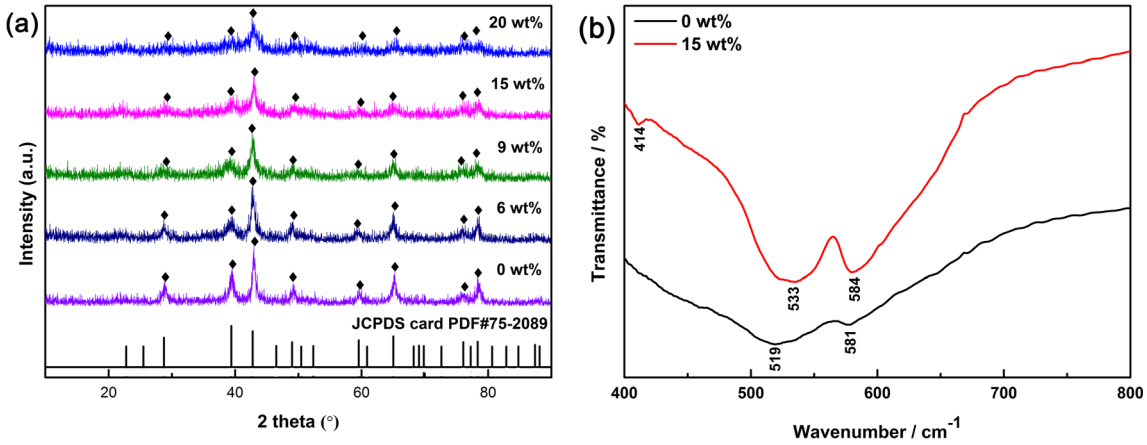

Fig. 1 XRD and FT-IR patterns of different mass ratios of Fe-doped $NiMnO_3$ nanosheet materials

operational potential window (V), I is the current (mA), m is the deposited mass on 1 cm^2 (mg), Δt (s) is the discharge time, D is the crystal size (nm), K is the Scherrer constant, γ is the X-ray wavelength, B is the half peak width (rad), and θ is the Prague diffraction angle (°).

Results and discussion

Figure 1a shows the XRD image of the Fe-doped $NiMnO_3$ electrode material with different Fe ion mass ratios. The characteristic peaks were mainly located at 28.8°, 39.4°, 42.8°, 49.0°, 59.6°, 65.0°, 76.1°, and 78.3°, which

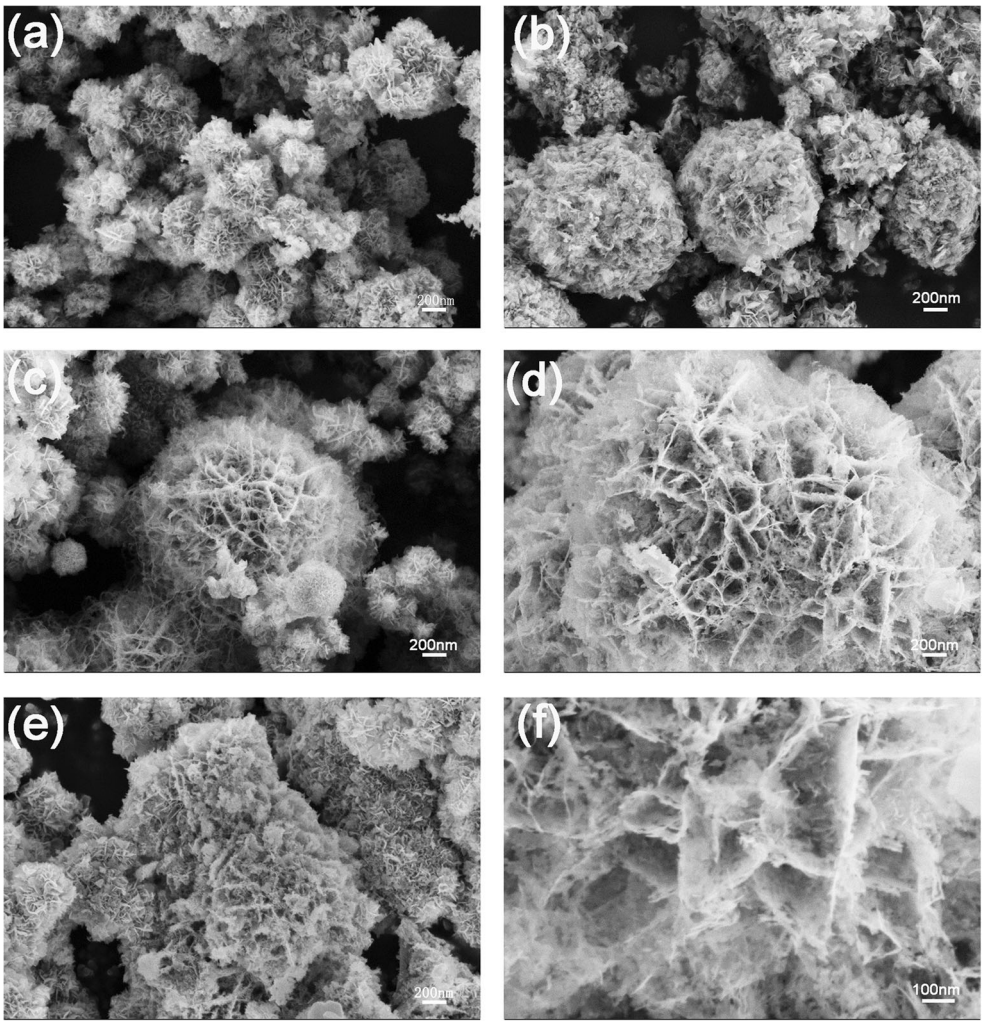

Fig. 2 Morphology of Fe-doped $NiMnO_3$ electrode material: 0 wt% (**a**), 6 wt% (**b**), 9 wt% (**c**), 15 wt% (**d**, **f**), and 20 wt% (**e**)

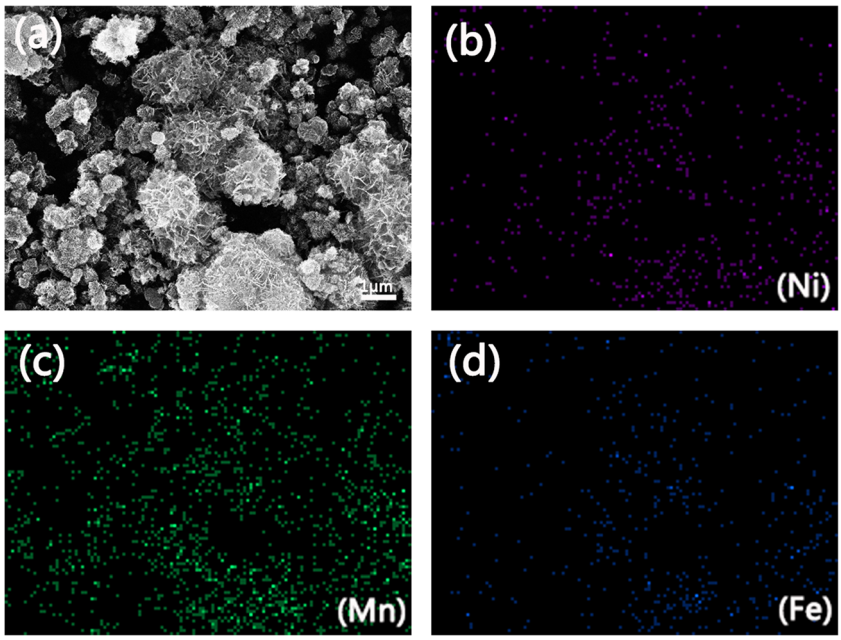

Fig. 3 EDX map of 15 wt% Fe-doped $NiMnO_3$ nanosheet electrode materials

corresponded to crystal plane (110), (121), (− 110), (120), (220), (231), (130), and (− 211) of $NiMnO_3$ (JCPDS card PDF#75-2089) [31], respectively. As indicated by the XRD curves, $NiMnO_3$ was successfully synthesized. With the doped Fe ion mass ratio increasing, the characteristic peaks exhibited no deviation, and no other characteristic peaks appeared. With increasing mass ratio, the half peak width (*B*) of the characteristic peaks became broader, and the crystal size

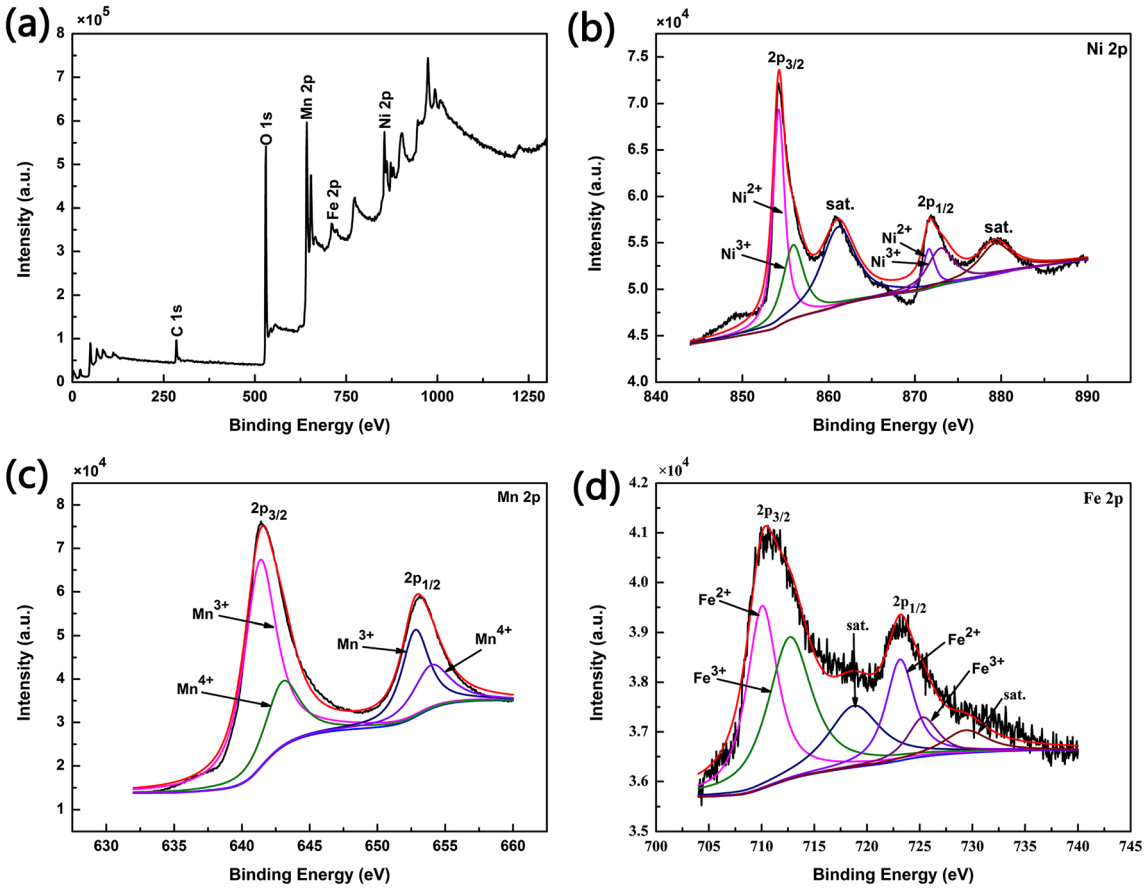

Fig. 4 XPS spectra of 15 wt% Fe-doped $NiMnO_3$ nanosheet/nanomesh electrode materials: **a** survey spectrum, **b** Ni 2p, **c** Mn 2p, and **d** Fe 2p

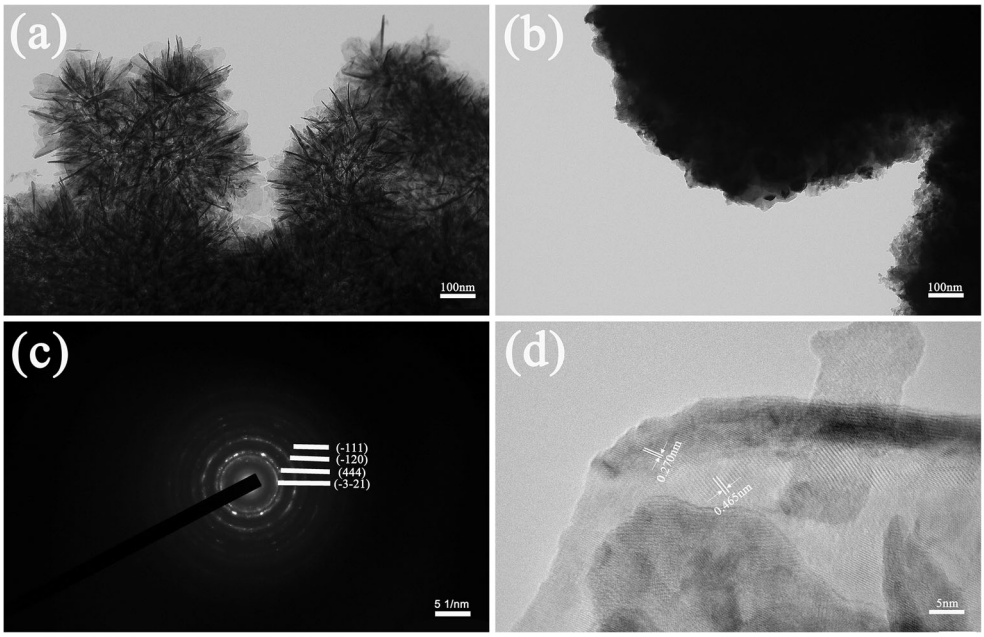

Fig. 5 TEM images and SAED pattern of 15 wt% Fe-doped $NiMnO_3$ nanosheet electrode materials

(D) decreased (Eq. (3), K, γ, θ constants). Given that doped Fe ion may replace the Mn ion in $NiMnO_3$, crystal size decreased. At increased number of doped of Fe ions, the crystallinity decreased. FT-IR spectra were used for the detection of functional groups on the surfaces of electrode materials. As shown in Fig. 1b, the 0 wt% Fe-doped $NiMnO_3$ electrode material has two absorption peaks at 519 cm^{-1} and 581 cm^{-1}. This result explained $NiMnO_3$ material has successful obtained. The 15 wt% Fe-doped $NiMnO_3$ sample has three absorption peaks at 414, 533, and 584 cm^{-1}. The absorption peaks at 414 cm^{-1} can be attributed to the Fe–O vibration, and the absorption peaks at 519 and 581 cm^{-1} can be attributed to the $NiMnO_3$ material [32–34]. The slight deviation of the absorption peaks may be attributed to the effect of Fe doping on the intrinsic functional groups.

The morphological changes of Fe-doped $NiMnO_3$ electrode material with increasing Fe ion mass ratio are displayed in Fig. 2a–f. The 0 wt% Fe sample is shown in Fig. 2a, and flower-like nanosheets were successfully synthesized. With the mass ratio of up to 6 wt% (Fig. 2b), the nanoball agglomeration of flower-like nanosheets can be detected. When the mass ratio reached 9 wt% (Fig. 2c) and 15 wt% (Fig. 2d), the nanosheets became porous and thin, and the latter linked to each other formed nanoballs. With the mass ratio reaching 15 wt%, nanosheets became thinner and more porous. At a mass ratio of 20 wt% (Fig. 2e), thin and small nanosheets grew on porous nanosheets. Figure 2f shows off the morphology of the 15 wt% sample at high magnification, and thin and porous nanosheets were found. The morphology changed due to the effect of Fe ion doping. When Fe ions are doped, Fe and Mn ions compete to form microspheres. After the rearrangement, nanoballs are eventually formed. When too much Fe ions are doped, nanoballs contact with each other and nanosheets grow on them. Hence, the morphology confirms the change after Fe doping, which is in accordance with the previous report on the Zn-doped Ni–MOF electrode material [35].

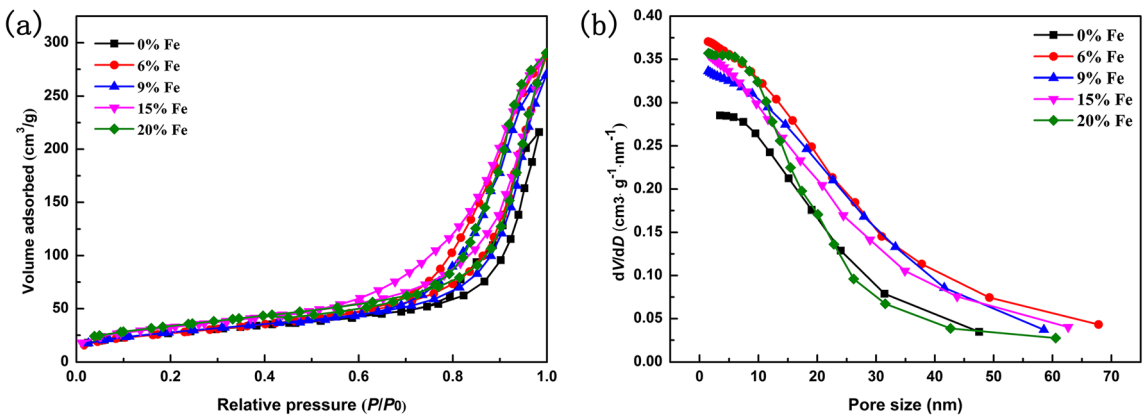

Fig. 6 Nitrogen adsorption–desorption isotherms and pore size distribution of Fe-doped $NiMnO_3$ electrode material with different Fe ion mass ratios

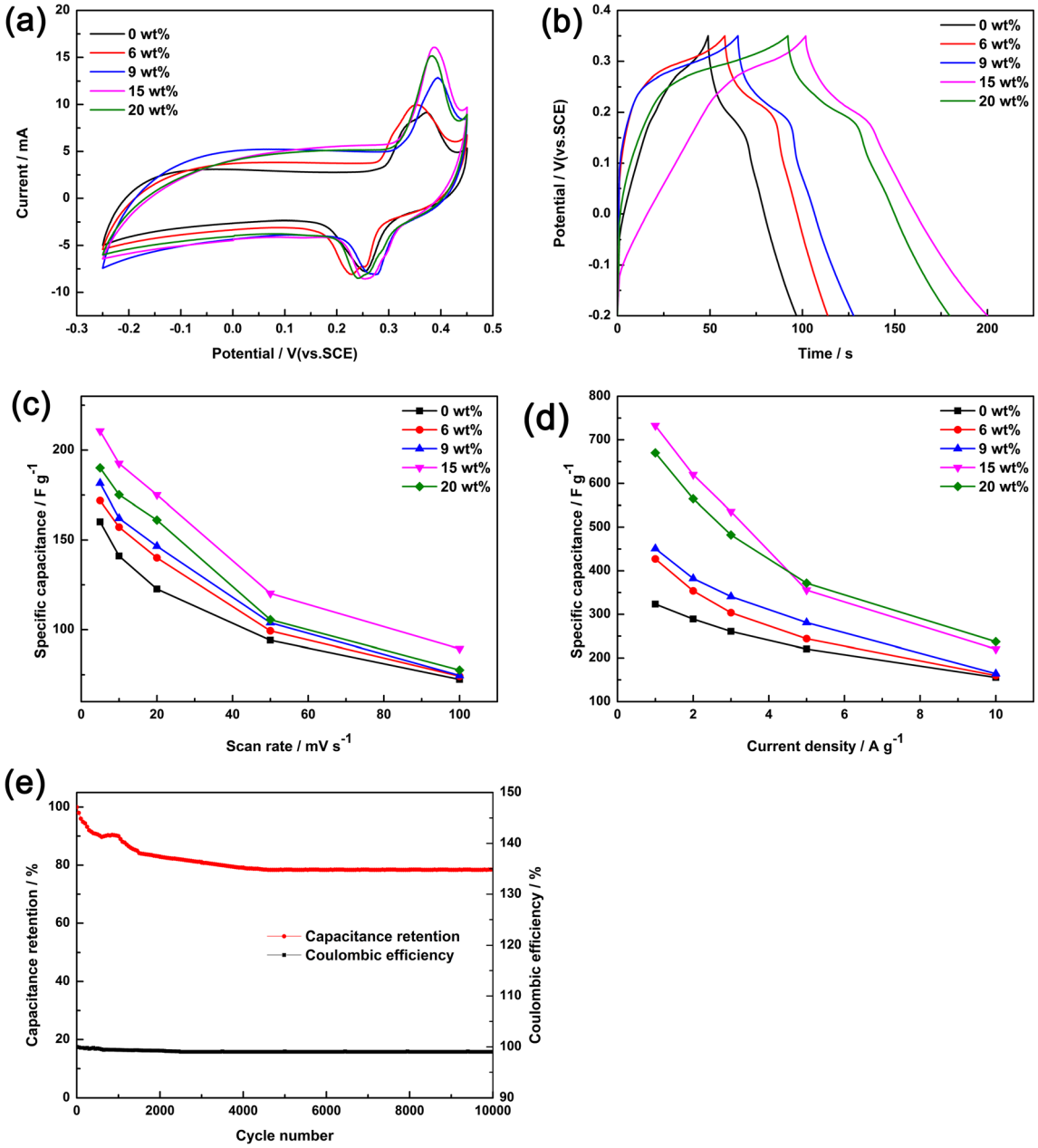

Fig. 7 Electrochemical performance of Fe-doped $NiMnO_3$ electrode material with different Fe ion mass ratios: **a** CV, **b** GCD, **c**, **d** specific capacitance, and **e** cycle life

For further investigating the chemical elemental characteristics of the electrode material, an EDX map (Fig. 3) was made. Figure 3a–d shows the elemental distribution of 15 wt% Fe-doped $NiMnO_3$ electrode material. Ni, Mn, and Fe were found to be uniformly distributed as shown in the EDX map, indicating that Fe ion was successfully doped into electrode materials.

The composition of the elements and the chemical state of 15 wt% Fe-doped $NiMnO_3$ nanosheets/nanomeshes electrode materials are shown in Fig. 4a–d. The survey spectra (Fig. 4a) showed C 1 s, O 1 s, Mn 2p, Fe 2p, and Ni 2p peaks, and no other peaks appeared, indicating that Fe ion was successfully doped into $NiMnO_3$ electrode materials. The Ni 2p peak is shown in Fig. 4b, and 2p3/2 and 2p1/2 peaks appeared at 854.11 and 871.58 eV, respectively. By Gaussian fitting method, Ni^{2+} corresponded to 854.20 and 871.63 eV, and Ni^{3+} corresponded to 855.88 and 872.97 eV. By the same method, for the Mn 2p peak, the 2p3/2 and 2p1/2 peaks appeared at 641.37 and 653.12 eV; Mn^{3+} corresponded to 641.33 and 652.78 eV, and Mn^{4+} corresponded to 643.00 and 653.96 eV. For the Fe 2p peak, the 2p3/2 and 2p1/2 peaks appeared at 710.64 and 723.22 eV, Fe^{2+} corresponded to 710.05 and 723.14 eV, and Fe^{3+} corresponded to 712.67 and 725.30 eV [34, 36–38]. Moreover, a couple of satellite peaks

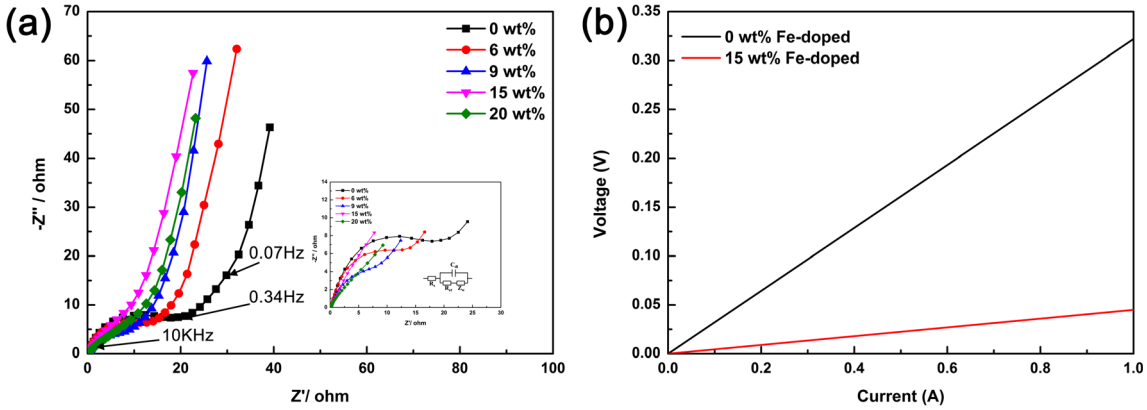

Fig. 8 **a** Nyquist plots of different electrode materials. **b** *I-V* plots of 15 wt% Fe-doped $NiMnO_3$ and $NiMnO_3$ powders

were observed in both Ni 2p and Fe 2p. According to the XPS results, the chemical state of elements was Ni^{2+}/Ni^{3+}, Mn^{3+}/Mn^{4+}, and Fe^{2+}/Fe^{3+}. The Fe-doped $NiMnO_3$ electrode material was successfully synthesized, corresponding to the XRD and FT-IR results.

TEM and selected area electron diffraction (SAED) pattern were used to further study the morphology and crystallinity of 15 wt% Fe (Fig. 5). From Fig. 5a, b, the morphology of 15% Fe consisted of two parts: flower-like and ball-like nanosheets, which corresponded to SEM images (Fig. 2). The SAED pattern shown in Fig. 5c exhibits well diffraction ring, which demonstrates the polycrystalline nature of the materials. Figure 5d shows the HR-TEM image and the lattice space were 0.270 and 0.465 nm, which were assigned to the (121) and (111) planes of $NiMnO_3$.

The specific surface area and pore size distribution of Fe-doped $NiMnO_3$ electrode material with different Fe ion mass ratios are shown in Fig. 6a, b. Figure 6a shows the nitrogen adsorption–desorption isotherms, where the Fe-doped $NiMnO_3$ electrode material belongs to typical type-IV isotherm and is an H3-type hysteresis loop. The specific surface areas of the samples were 74.9, 97.2, 101.92, 118.23, and 122.8 $m^2\ g^{-1}$, corresponding to 0, 6, 9, 15, and 20 wt%, respectively. With the increasing of Fe ion doping, the morphology of the obtained material changed from flower-like nanosheets to ball-like porous and thin nanosheets, and its specific surface area also gradually increased.

The electrochemical performance of the $NiMnO_3$ electrode material having different mass ratios of Fe ion was tested in 6 mol/L KOH electrolyte with three-electrode systems (Fig. 7). Figure 7a shows the CV curves of different samples at a scan rate of 10 mV s^{-1} between − 0.25 and 0.45 V. A pair of redox peaks appeared on the CV curves, indicating that the Fe-doped $NiMnO_3$ electrode is a pseudocapacitive material. Figure 7b displays the GCD curves of different samples in a potential range of − 0.20–0.35 V at a current density of 3 A g^{-1}. The platform at the discharge time confirms that the prepared materials exhibited pseudocapacitive characteristics, corresponding to the CV curve results. A negligible IR drop indicated smaller resistance compared with other materials. The specific capacitance of electrode materials was calculated by CV and GCD curves according to Eqs. (1) and (2). From Fig. 7c, d, the 15 wt% Fe-doped material possessed maximum specific capacitance. At a scan rate of 5 mV s^{-1}, the specific capacitance was 210.6 F g^{-1}. At a current density of 1 A g^{-1}, the specific capacitance was 732.7 F g^{-1}. The capacitance retention and Coulombic efficiency as important factors are presented in Fig. 7e. The results show that the specific capacitance retention of the 15 wt% Fe-doped $NiMnO_3$ electrode material after 4000 charge/discharge cycles was 78.3%, and no obvious change occurred. The Coulombic efficiency reached 99.1% after 2500 charge/discharge cycles, and no large change was observed from beginning to ending. The result indicated 15 wt% Fe-doped $NiMnO_3$ electrode material possessing good cycle stability.

The Nyquist plots of the EIS spectra illustrated the resistance of systems (Fig. 8a). Generally speaking, the Nyquist plots are divided into two parts: semicircular at higher

Table 1 Comparison of *R*s and *R*ct values of Fe-doped $NiMnO_3$

Electrode material	Equivalent series resistance (*R*s) Ω	Charge-transfer resistance (*R*ct) Ω
0 wt% Fe doped	0.2087	17.79
6 wt% Fe doped	0.1755	14.87
9 wt% Fe doped	0.1199	11.85
15 wt% Fe doped	0.0668	8.8
20 wt% Fe doped	0.0917	9.88

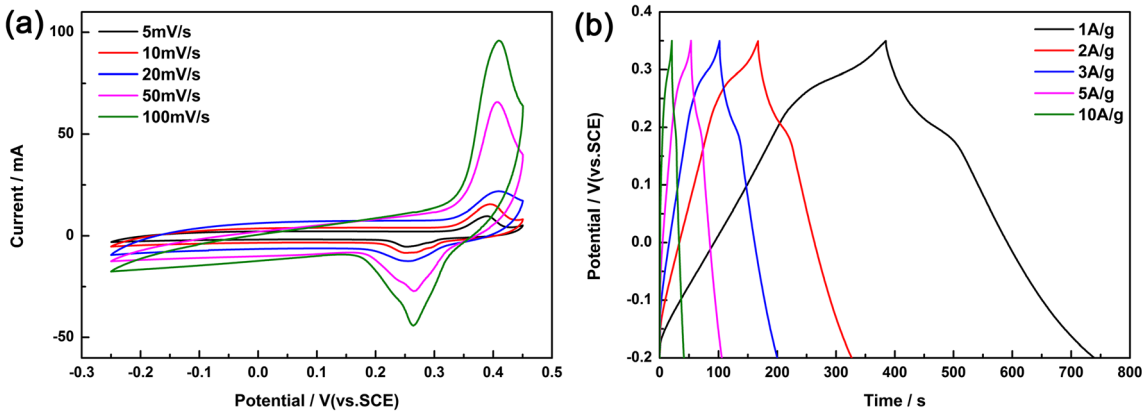

Fig 9 Electrochemical performance of 15 wt% mass ratio Fe-doped $NiMnO_3$ electrode material: **a** CV and **b** GCD curves

frequency regions and straight line at lower frequency regions [39]. At high frequency, the intercept of the semicircle on the real axis represents the equivalent series resistance (*R*s), and the diameter corresponds to the charge-transfer resistance (*R*ct) [40, 41]. From Table 1, the *R*s values of 0 and 15 wt% Fe doping are 0.2087 and 0.0668 Ω, respectively, and the *R*ct values are 17.79 and 8.8 Ω, respectively. From Fig. 8b, one can see that 15 wt% Fe-doped $NiMnO_3$ increased the conductivity of $NiMnO_3$ electrode material from 1.236×10^{-6} to 8.732×10^{-4} S m^{-1}.

The 15 wt% Fe Fe-doped $NiMnO_3$ electrode material possessed maximum specific capacitance and stable cycle life. The electrochemical performance at high scanning rates and current densities is shown in Fig. 9. From the CV curves, with increasing scanning rates, the redox peak positions hardly became broader, which indicated less polarization of the electrode material. With increasing scanning rates, the shape of the CV curves exhibited no obvious change, indicating that 15 wt% possessed outstanding rate performance. Figure 8b describes the GCD curves at different current densities. At a current density from 1 to 10 A g^{-1}, the specific capacitance was 732.7, 620.2, 535.5, 355.5, and 220.3 F g^{-1}, respectively. The capacitance retention was approximately 30.1%, which was attributed to the high surface area morphology and low resistance of electrode material.

The superior electrochemical performance of 15 wt% Fe-doped $NiMnO_3$ electrode material can be attributed to the following reasons. First, part of the Mn atoms can be replaced by some Fe atoms, and the synergism of Ni–Fe–Mn can generate some holes and increase the conductivity. Second, the XRD result indicated that Fe ion doping will damage or even destroy the crystal structure. This amorphous surface structure provides more active sites to improve electrochemical performance [42–44]. Third, the sufficient surface area can provide more transport channels for electrolyte ions and redox reaction sites. Furthermore, the reasonable pore distribution (from 3 to 65 nm) can reduce the obstacle when the ions are transported, leading to high specific capacitance and superior cycling life.

Conclusions

Fe-doped $NiMnO_3$ electrode material was successfully prepared by microwave-assisted hydrothermal method. The results demonstrated that the morphology of the material changed from flower-like nanosheets to ball-like porous and thin nanosheets at increased Fe ion doping mass ratio, and the 15 wt% Fe ion-doped $NiMnO_3$ electrode material exhibited optimum electrochemical performance. In 6 mol/L KOH electrolyte, the specific capacitance reached 732.7 F g^{-1} at a current density 1 A g^{-1}, and the capacitance retention was approximately 78.3% after 10,000 cycles at 3 A g^{-1}. The morphology of the ball-like porous and thin nanosheets exhibited enlarged specific surface areas and active sites, which improved the electrochemical performance of the material. Therefore, 15 wt% Fe-doped $NiMnO_3$ electrode material has high potential as new-generation high-performance supercapacitors.

Funding information This work was financially supported by the National Key Research and Development Program of China (2016YFB0101206) and the Dalian Science and Technology Innovation Funds (2018J12GX053).

References

1. Aricò AS, Bruce P, Scrosati B, Tarascon JM, Van SW (2005) Nanostructured materials for advanced energy conversion and storage devices. Nat Mater 4(5):366–377
2. Miller JR, Simon P (2008) Electrochemical capacitors for energy management. Science 321(5889):651–652
3. Dubal DP, Gomez-Romero P, Sankapal BR, Holze R (2015) Nickel cobaltite as an emerging material for supercapacitors: an overview. Nano Energy 11:377–399
4. Umeshbabu E, Rajeshkhanna G, Justin P, Rao GR (2015) Synthesis of mesoporous NiCo2O4-rGO by solvothermal method for charge storage applications. RSC Adv 5(82):66657–66666
5. Chen Q, Meng Y, Hu C, Zhao Y, Shao H, Chen N, Qu L (2014) MnO2-modified hierarchical graphene fiber electrochemical supercapacitor. J Power Sources 247:32–39

6. Fu Y, Cai X, Wu H, Lv Z, Hou S, Peng M, Yu X, Zou D (2012) Fiber supercapacitors utilizing pen ink for flexible/wearable energy storage. Adv Mater 24(42):5713–5718
7. Yu C, Masarapu C, Rong J, Wei B, Jiang H (2010) Stretchable supercapacitors based on buckled single-walled carbon-nanotube macrofilms. Adv Mater 21:4793–4797
8. Lu X, Yu M, Zhai T, Wang G, Xie S, Liu T, Liang C, Tong Y, Li Y (2013) High energy density asymmetric quasi-solid-state supercapacitor based on porous vanadium nitride nanowire anode. Nano Lett 13(6):2628–2633
9. Huang ZD, Zhang B, Oh SW, Zheng QB, Lin XY, Yousefi N, Kim JK (2012) Self-assembled reduced graphene oxide/carbon nanotube thin films as electrodes for supercapacitors. J Mater Chem 22(8):3591–3599
10. Ramya R, Sivasubramanian R, Sangaranarayanan MV (2013) Conducting polymers-based electrochemical supercapacitors—Progress and prospects. Electrochim Acta 101:109–129
11. Gao X, Zhang Y, Huang M, Li F, Hua C, Yu L, Zheng H (2014) Facile synthesis of Co3O4@NiCo2O4 core–shell arrays on Ni foam for advanced binder-free supercapacitor electrodes. Ceram Int 40(10):15641–15646
12. Kang J, Hirata A, Kang L, Zhang X, Hou Y, Chen L, Li C, Fujita T, Akagi K, Chen M (2013) Enhanced supercapacitor performance of MnO2 by atomic doping. Angew Chemie 52(6):1664–1667
13. Cai G, Tu J, Zhou D, Zhang J, Xiong Q, Zhao X, Wang X, Gu C (2013) Multicolor electrochromic film based on TiO2@polyaniline core/shell nanorod array. J Phys Chem C 117(31):15967–15975
14. Zhou C, Zhang Y, Li Y, Liu J (2013) Construction of high-capacitance 3D CoO@polypyrrole nanowire array electrode for aqueous asymmetric supercapacitor. Nano Lett 13(5):2078–2085
15. Tian W, Wang X, Zhi C, Zhai T, Liu D, Zhang C, Golberg D, Bando Y (2013) Ni(OH)2 nanosheet@Fe2O3 nanowire hybrid composite arrays for high-performance supercapacitor electrodes. Nano Energy 2(5):754–763
16. Zhang X, Shi W, Zhu J, Zhao W, Ma J, Mhaisalkar S, Maria TL, Yang Y, Zhang H, Hng HH (2010) Synthesis of porous NiO nanocrystals with controllable surface area and their application as supercapacitor electrodes. Nano Res 3(9):643–652
17. Xiao Y, Liu S, Feng L, Zhang A, Zhao J, Fang S, Jia D (2012) 3D Hierarchical Co3O4 Twin-Spheres with an Urchin-Like Structure: Large-scale synthesis, multistep-splitting growth, and electrochemical pseudocapacitors. Adv Funct Mater 22:4052–4059
18. Du W, Liu R, Jiang Y, Lu Q, Fan Y, Gao F (2013) Facile synthesis of hollow Co3O4 boxes for high capacity supercapacitor. J Power Sources 227:101–105
19. Saravanakumar B, Purushothaman KK, Muralidharan G (2012) Interconnected V2O5 nanoporous network for high-performance supercapacitors. ACS Appl Mater Interfaces 4(9):4484–4490
20. Wee G, Soh HZ, Yan LC, Mhaisalkar SG, Srinivasan M (2010) Synthesis and electrochemical properties of electrospun V2O5 nanofibers as supercapacitor electrodes. J Mater Chem 20(32): 6720–6725
21. Kulal PM, Dubal DP, Lokhande CD, Fulari VJ (2011) Chemical synthesis of Fe2O3 thin films for supercapacitor application. J Alloys Compd 509(5):2567–2571
22. Zhu Y, Wu Z, Jing M, Hou H, Yang Y, Zhang Y, Yang X, Song W, Jia X, Ji X (2014) Porous NiCo2O4 spheres tuned through carbon quantum dots utilised as advanced materials for an asymmetric supercapacitor. J Mater Chem A 3:866–877
23. Wang C, Zhou E, He W, Deng X, Huang J, Ding M, Wei X, Liu X, Xu X (2017) NiCo2O4-based supercapacitor nanomaterials. Nanomaterials 7:41
24. Zhang G, Lou XW (2013) General solution growth of mesoporous NiCo2O4 nanosheets on various conductive substrates as high-performance electrodes for supercapacitors. Adv Mater 25(7): 975–975
25. Tholkappiyan R, Naveen AN, Sumithra S, Vishista K (2015) Investigation on spinel MnCo2O4 electrode material prepared via controlled and uncontrolled synthesis route for supercapacitor application. J Mater Sci 50(17):5833–5843
26. Che H, Liu A, Mu J, Wu C, Zhang X (2016) Template-free synthesis of novel flower-like MnCo2O4 hollow microspheres for application in supercapacitors. Ceram Int 42(2):2416–2424
27. Karthikeyan K, Kalpana D, Renganathan NG (2009) Synthesis and characterization of ZnCo2O4 nanomaterial for symmetric supercapacitor applications. Ionics 15(1):107–110
28. Guan B, Guo D, Hu L, Zhang G, Fu T, Ren W, Li J, Li Q (2014) Facile synthesis of ZnCo2O4 nanowire cluster arrays on Ni foam for high-performance asymmetric supercapacitors. J Mater Chem A 2(38):16116–16123
29. Cai D, Wang D, Liu B, Wang Y, Liu Y, Wang L, Li H, Huang H, Li Q, Wang T (2013) Comparison of the electrochemical performance of NiMoO4 nanorods and hierarchical nanospheres for supercapacitor applications. Appl Mater Interfaces 5(24):12905–12910
30. Xiao J, Wan L, Yang S, Xiao F, Wang S (2014) Design hierarchical electrodes with highly conductive NiCo2S4 nanotube arrays grown on carbon fiber paper for high-performance pseudocapacitors. Nano Lett 14(2):831–838
31. Kakvand P, Rahmanifar MS, El-Kady MF, Pendashteh A, Kiani MA, Hashami M, Najafi M, Abbasi A, Mousavi MF, Kaner RB (2016) Synthesis of NiMnO3/C nano-composite electrode materials for electrochemical capacitors. Nanotechnol 27(31):315401
32. Mehandjiev D, Naydenov A, Ivanov G (2001) Ozone decomposition, benzene and co oxidation over NiMnO3-ilmenite and NiMn2O4-spinel catalysts. Appl Catal A 206(1):13–18
33. Lassoued A, Lassoued MS, Dkhil B, Ammar S, Gadri A (2018) Synthesis, structural, morphological, optical and magnetic characterization of iron oxide (α-Fe2O3) nanoparticles by precipitation method: effect of varying the nature of precursor. Phys E (Amsterdam Neth) 97:328–334
34. Guan Y, Yin C, Cheng X, Liang X, Diao Q, Zhang H, Lu G (2014) Sub-ppmH2S sensor based on YSZ and hollow balls NiMn2O4 sensing electrode. Sensors Actuators B Chem 193:501–508
35. Chen Y, Ni D, Yang X, Liu C, Yin J, Cai K (2018) Microwave-assisted synthesis of honeycomblike hierarchical spherical Zn-doped Ni-MOF as a high-performance battery-type supercapacitor electrode material. Electrochim Acta 278:114–123
36. Zhang M, Guo S, Zheng L, Zhang G, Hao Z, Kang L, Liu ZH (2013) Preparation of NiMn2O4 with large specific surface area from an epoxide-driven sol−gel process and its capacitance. Electrochim Acta 87:546–553
37. Li W, Cui X, Zeng R, Du G, Sun Z, Zheng R, Ringer SP, Dou SX (2015) Performance modulation of α-MnO2 nanowires by crystal facet engineering. Sci Rep 5(1):8987
38. Yamashita T, Hayes P (2008) Analysis of XPS spectra of Fe2+ and Fe3+ ions in oxide materials. Appl Surf Sci 254(8):2441–2449
39. Belous A, Kolbasov G, Kovalenko L, Boldyrev E, Kobylianska S, Liniova B (2018) All solid-state battery based on ceramic oxide electrolytes with perovskite and NASICON structure. J Solid State Electrochem 22(8):2315–2320
40. Wang L, Wang X, Xiao X, Xu F, Sun Y, Li Z (2013) Reduced graphene oxide/nickel cobaltite nanoflake composites for high specific capacitance supercapacitors. Electrochim Acta 111:937–945
41. Patil AM, Lokhande AC, Chodankar NR, Kumbhar VS, Lokhande CD (2016) Engineered morphologies of β-NiS thin films via anionic exchange process and their supercapacitive performance. Mater Des 97:407–416
42. Li B, Xiao Z, Chen M, Huang Z, Tie X, Zai J, Qian X (2017) Rice husk-derived hybrid lithium-ion capacitors with ultra-high energy. J Mater Chem A 5(46):24502–24507

43. Fang Z, Peng L, Qian Y, Zhang X, Xie Y, Cha JJ et al (2018) Dual tuning of ni-co-a (a = p, se, o) nanosheets by anion substitution and holey engineering for efficient hydrogen evolution. J Am Chem Soc 140:15

44. Chen M, Li B, Liu X, Zhou L, Yao L, Zai J, … & Yu X (2018) Boron-doped porous Si anode materials with high initial coulombic efficiency and long cycling stability. J Mater Chem A 6(7): 3022–3027